International Journal of Biological Macromolecules 276 (2024) 133812

Contents lists available at ScienceDirect

International Journal of Biological Macromolecules

journal homepage: www.elsevier.com/locate/ijbiomac

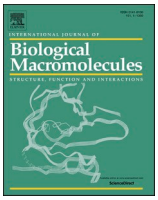

# Ferritin at different iron loading: From biological to nanotechnological applications

Caterina Ricci [a,*], Gerardo Abbandonato [b], Matteo Giannangeli [c], Lauren Matthews [d], László Almásy [e], Barbara Sartori [f], Alessandro Podestà [g], Alessandro Caselli [c], Alberto Boffi [h], Gerhard Thiel [b], Elena Del Favero [a], Anna Moroni [b]

[a] Biometra Department, University of Milan, Milan, Italy
[b] Department of Biosciences, University of Milan, Milan, Italy
[c] Department of Chemistry, University of Milan, Milan, Italy
[d] ESRF, The European Synchrotron, 71 avenue des Martyrs, 38043 Grenoble, France
[e] HUN-REN Centre for Energy Research, POB 49, Budapest 1525, Hungary
[f] Institute of Inorganic Chemistry, Graz University of Technology, Stremayrgasse 9/4, Graz, Austria
[g] Department of Physics "Aldo Pontremoli", University of Milan, Milan, Italy
[h] Department of Biochemical Sciences, Sapienza University of Rome, Italy

ARTICLE INFO

*Keywords:*
Ferritin
Iron loading
Magnetogenetics

ABSTRACT

The characterization of the structure of ferritin in solution and the arrangement of iron stored in its cavity are intriguing subjects for both cell biology and applied science, since the protein structure, stability, and easiness of production make it an ideal tool for biomedical applications. We characterized the ferritin structure over a wide range of iron loadings by visible light, X-ray, and neutron scattering techniques. We found that the arrangement of iron ions inside the protein cage resulted in a more disposable arrangement at lower loading factors and then in a crystalline structure. At very high iron content the inner core is composed of magnetite more than ferrihydrite, and the shell of the protein is elastically deformed by the iron crystal growth in an ellipsoidal arrangement. The application of an external radiofrequency (RF) magnetic field affected ferritins at low iron loading factors. Notably the RF modified the iron disposition towards a more dispersed arrangement. The structural characterization of the ferritin at different LFs and in presence of magnetic fields provides useful insights into their physiological behaviour and can help in the design and fine-tuning of ferritin-based nanosystems for biotechnological applications.

## 1. Introduction

Iron is a crucial element in many cellular and physiological processes and is found in many biological systems. Iron homeostasis is tightly regulated and occurs both at the cellular and the systemic levels. Moreover, each cell or tissue type has a different iron set point for homeostasis that reflects their specific role: for example, animal red blood cells require more iron than epithelial cells due to the synthesis of haemoglobin [1].

Iron regulation is controlled by the biosynthesis of storage compartments that respond to fluctuations in incoming iron as well as to pathological changes in iron metabolism. The main iron storage protein is ferritin, which is able to bind iron, oxidizing and storing it inside its hollow spherical structure; we call apo-ferritin the empty protein whereas holo-ferritin when loaded with iron. Ferritin, whose expression is controlled by the iron amount in the environment, catalyses toxic reactions such as the Fenton and Haber–Weiss reactions leading to the production of toxic free radicals [2]. Ferritin's structure is strictly conserved [3]. Bacterioferritins and eukaryotic ferritins are composed of 24 identical or similar subunits that form a roughly spherical shell of about 12 nm in diameter, with an inner cavity of about 8 nm. The hollow cavity is commonly known to store up to 4500 iron atoms [4]. Iron loading occurs at eight hydrophilic channels formed by three subunits each [5]. The subunits can carry a ferroxidase centre buried inside a four-helix bundle. The ferroxidase centre provides the catalytic activity necessary to oxidize $Fe^{2+}$ to $Fe^{3+}$and accumulate it inside the cavity, via

* Corresponding author.
*E-mail address:* caterina.ricci@unimi.it (C. Ricci).

https://doi.org/10.1016/j.ijbiomac.2024.133812
Received 21 May 2024; Received in revised form 8 July 2024; Accepted 9 July 2024
Available online 19 July 2024

ferrihydrite nucleation/gateway sites [6,7]. The protein cage directs the formation of the relatively unstable ferrihydrite. Crystallinity, magnetic properties, and reactivity of the metal core depend strongly on the size, structure, and composition of the ferrihydrite particles, which vary depending on the mineralization conditions and biological source of native ferritins [8,9].

Due to the great number of potential applications of ferritins [10–13], there is a growing demand for understanding the fundamentals of ions internalisation and nanoparticle growth in protein environment. From a nanotechnological point of view, ferritin nanocage cavities can be used as cargo for cisplatin, carboplatin and oxaliplatin, or even SPION, which are largely used in clinics for the treatment of numerous types of cancer [14–17]. For therapeutic and diagnostic purposes, however, also the distinctive natural features of ferritins can be exploited. Interestingly, ferritins found in Alzheimer's disease patients show a higher amount of cubic crystalline phases consistent with magnetite and wüstite, comparing to the hexagonal ferrihydrite phase found in the healthy cells [18]. Recently, ferritins were exploited to control the gating of ion channels using external non-harmful magnetic fields as stimuli because they are able to penetrate deeply into tissues (magnetogenetics). A modified TRPV1 channel with an N-terminal fusion to an anti-GFP nanobody was co-expressed with a ferritin protein with an N-terminal fusion to GFP. This resulted in the tethering of GFP-tagged ferritin to the modified TRPV1 at the cell membrane. The engineered ion channel was tested in vitro and in vivo on diabetic nude mice showing in both cases that the magnetic field could gate the ion channel [19,20]. A vigorous debate is ongoing about the physical mechanisms of ion channel activation by means of external magnetic fields [21,22].

The question of how, in what form and in which amount iron is eventually stored as a core inside the ferritin and how the system responds, in physiological condition, to an external magnetic field therefore rises interest for bioengineering and therapeutical applications. In this work, we investigated the structure of *Pyrococcus furiosus* ferritin, under a wide range of iron loading conditions (from 50 ions to saturation). Scattering techniques allowed us to observe the core-shell structure of the proteins in solution, quantify the distribution of iron among the protein population and find out the arrangement of iron ions stored inside the ferritin shell. This characterization provides a portrayal of ferritin behaviour and of the possible modifications of the protein cage in different regimes of iron loading. Understanding the structure of ferritins at low loading factors can give insights in their behaviour in physiological conditions, while at high loading factors it can describe a state more suitable for nanotechnological applications. The potential use of iron-loaded ferritins as magnetic materials is also analysed in this respect.

## 2. Materials and methods

### 2.1. Protein production

*E. coli* cells, containing the *Pyrococcus furiosus* Ferritin (PfFt) plasmid, were grown and induced with 1 mM IPTG (isopropyl-β-D-1-thio-galactopyranoside) at $OD_{600}$ = 0.6. Cells were harvested by centrifugation 3 h post induction at 37 °C. Cells harvested from 1 L culture were resuspended in 20 mM HEPES buffer, pH 7.5, containing 200 mM NaCl, 1 mM TCEP (tris(2-carboxiethyl) phosphine), and a cOmplete™ Mini Protease Inhibitor Cocktail Tablet (Roche). Cells were disrupted by sonication and the soluble fraction was purified by heat treatment at 78 °C for 10 min. Denatured *E. coli* proteins were removed by centrifugation at 15000 rpm at 4 °C for 1 h. The soluble protein was further purified by ammonium sulphate precipitation. The precipitated fraction at 70 % ammonium sulphate was resuspended in 20 mM HEPES, 50 mM MgCl2, pH 7.5 and dialyzed versus the same buffer. As a final purification step, the protein was loaded onto a HiLoad 26/600 Superdex 200 pg column previously equilibrated in the same buffer using an ÄKTA-Prime system (GE Healthcare). The purified protein was concentrated to obtain the final protein preparation of 1 mg/mL and protein concentration was calculated by measuring the UV spectrum using an extinction coefficient of 32–400 $M^{-1}$ $cm^{-1}$. Protein yield was ~40 mg $L^{-1}$ culture.

### 2.2. Protein loading

To provide Fe(II) to the protein, a 10 mM solution of $FeSO_4$ and a 0.5 mM HCl solution, were added dropwise to 2 mL of a solution of the apoferritin from *Pyrococcus furiosus* 1 mg/mL in HEPES 50 mM at pH 7. In order to avoid the premature oxidation of Fe(II) ions, the $FeSO_4$ solution was degassed and kept under $N_2$ atmosphere during the whole procedure. The pH of the ferritin was constantly monitored during the addition of $FeSO_4$ and kept between pH 6.5 and 7.5 adding dropwise small aliquots of a 0.1 M solution of NaOH. To obtain ferritins loaded at various loading factors, different amounts of $FeSO_4$ solution were added to the 2 mL protein solution: 20,8 μL, 41,7 μL, 125,1 μL, 291.1 μL and 1876 μL. At the end of the last addition, the reaction is left to continue under stirring for another 15–30 min. The sample is then centrifuged 20 min at 16000 rpm at 4 °C. The supernatant is recovered, then filtered, exchanged (HEPES 20 mM, NaCl 150 mM, at pH = 7) and concentrated. The sample is stored at 4 °C after sterile filtration under a hood.

### 2.3. Light scattering

Protein solutions were analysed at final concentrations of 0.1 mg/mL in 50 mmol TRIS buffer, pH 7.4, at 22 °C by dynamic laser light scattering (DLS). The homemade LS apparatus is described elsewhere [23]. The correlation function of the scattered intensity (measured by DLS) returns the translational diffusion coefficients of particles in solution and then their average hydrodynamic diameter via the Stokes-Einstein relation. DLS data analysis was carried out using the method of cumulants, suitable to detect the evolution of the weight-average hydrodynamic size of particles in solution, and the non-negative least squares method, to determine their size distribution.

### 2.4. Small angle scattering

To gain insight on the protein conformation and on the iron loading, a complementary use of X-rays and neutrons (SAXS and SANS) techniques has been exploited [24,25].

The data obtained from the SAS experiments depend on the difference between the scattering length density (SLD) of each homogeneous domain that constitutes the particles in solution and the homogeneous SLD of the solvent. The two probes utilised here interact differently with matter: X-rays interact with electron density, and neutrons with the atomic nuclei. This leads to different SLD values, and thus, different contrasts in the material under investigation, providing a complementary set of information using the two techniques. In our particular case, SANS analysis defines nicely the conformation of the ferritin shell, since neutrons are less sensitive to iron scattering than X-rays. Actually, for SANS, the SLD of the protein lies around $2 \cdot 10^{10}$ $cm^{-2}$, while ferrihydrite and magnetite SLDs resemble the one of the deuterated water (see Table 1) [26]. On the other hand, SAXS visualizes better the iron core and thus the organization of iron inside the shell, as its scattering length density overwhelms the one of the protein shell.

**Table 1**
Scattering length densities for X-rays and neutrons probes from literature [26,47].

| | Buffer ($H_2O$/$D_2O$) SLD ($cm^{-2}$) | Average protein SLD ($cm^{-2}$) | Ferrihydrite SLD ($cm^{-2}$) | Magnetite SLD ($cm^{-2}$) |
|---|---|---|---|---|
| SAXS | $9.3 \cdot 10^{10}$ | $12.4 \cdot 10^{10}$ | $35 \cdot 10^{10}$ | $41.5 \cdot 10^{10}$ |
| SANS | $6.34 \cdot 10^{10}$ | $2.3 \cdot 10^{10}$ | $6.5 \cdot 10^{10}$ | $6.98 \cdot 10^{10}$ |

#### 2.4.1. Small angle X-ray scattering (SAXS)

SAXS experiments on apo and holo-ferritins were performed on the ID02 beamline at ESRF (Grenoble, France, 10.15151/ESRF-ES-281427365 [27]) and at different loaded ferritins on the SAXS beamline at ELETTRA (Trieste, Italy [28]). The scattered intensities lay for both the beamlines in the momentum transfer (q) range $7.10^{-2} \leq q \leq 0.7$ Å$^{-1}$ being $q = (4\pi/\lambda)\sin(\theta/2)$, where θ is the scattering angle and λ is the X-ray wavelength ($\lambda_{ESRF} = 0.101$ nm, $\lambda_{ELETTRA} = 0.154$ nm). All measurements were performed at room temperature. Ten short frames (0.1 s at ESRF, 1 s at ELETTRA) were acquired and averaged, after check, to avoid any radiation damage. The acquired 2D patterns were normalised and azimuthally averaged to obtain the 1D SAXS profiles. Several spectra relative to the empty cells and the solvent were taken, carefully compared and subtracted to each sample spectrum to obtain the excess scattered intensity in absolute units I(q).

#### 2.4.2. Small angle neutron

Scattering (SANS). SANS measurements were recorded with the "Yellow Submarine" diffractometer operating at the Budapest Neutron Centre [29]. Two sample-detector distances of 1.2 and 5.3 m and a quasi-monochromatic neutron wavelength of 0.62 nm allowed us to cover a q-range of 0.01–0.26 Å$^{-1}$. Liquid samples were filled in quartz cells with a 2 mm path length, and the measurements were recorded at room temperature. The raw data were corrected for sample transmission, cell and room background scattering, and the absolute intensity scale was calibrated by the level of incoherent scattering from a $H_2O$ sample.

### 2.5. Data analysis

SAXS and SANS curves at different loading factors were analysed by the GENFIT software tool [30], which contains a wide list of structural models for describing the size and shape of particles in solution, with or without interparticle correlation effects. The best fit curve $I(q)$ is written as $I(q) = \kappa P(q)S(q) + B$, where $P(q)$ is the form factor, $S(q)$ is the effective structure factor, κ and B are a scaling factor and flat background, respectively. In our case of dilute system $S(q) \simeq 1$, thus the bare form factor has been considered. The parameters of the models (such as thicknesses, electron densities, etc.) are found by minimizing the functional $\chi^2$ correlated to the number of recorded data points at different q values and the experimental standard deviation of the $i^{th}$ point. During the fitting procedure, the scattering length density of the solvent and of the protein shell has been kept constant, while the other parameters were variable. To reduce the uncertainties on the parameters a global fitting was performed for SAXS and SANS measurements of the same samples and for SANS measurements at different contrast.

Two models have been used in this characterization. The first is a core shell sphere, described as:

$$I(q,R,\delta) = \left\{ \frac{4\pi}{3} \left[ (\rho_e - \rho_0)(R+\delta)^3 \Phi(q(R+\delta)) + (\rho_i - \rho_e) R^3 \Phi(qR) \right] \right\}^2$$

$$\Phi(x) = 3\frac{\sin x - x\cos x}{x^3}$$

The model parameters are the inner core radius R, the shell thickness δ, and their scattering length densities, $\rho_i, \rho_e$, and the solvent scattering length density $\rho_0$. The extension to a three-level sphere is straightforward.

The second model is a three-axial ellipsoid:

$$I(q) = \frac{2}{\pi} \int_0^{\frac{\pi}{2}} \int_0^{\frac{\pi}{2}} \sin\beta \, d\beta \, d\alpha \left[ \frac{4\pi}{3} \Sigma_{k=0}^{1} (A+k\delta)(B+k\delta)(C+k\delta)(\rho_{k+1} - \rho_k) \, \Phi\left( q \left\{ \left[ (A+k\delta)^2 \sin^2\alpha + (B+k\delta)^2 \cos^2\alpha \right] \sin^2\beta + (C+k\delta)^2 \cos^2\beta \right\}^{\frac{1}{2}} \right) \right]^2$$

The model parameters are: the semiaxes of the inner ellipsoid, A, B and C; the shell thickness δ; the scattering length densities of solvent, ellipsoidal shell and inner ellipsoid $\rho_0, \rho_1, \rho_2$, respectively. Also, in this case the extension to multishell structure is straightforward.

3D structure modelling was performed using ATSAS vs. 3.1.1 software package [31]. The IFT method from GNOM software was applied to compute the p(r) function, defined as:

$$p(r) = \frac{r^2}{2\pi^2} \int_0^{\infty} q^2 I(q) \frac{\sin(qr)}{qr} dq$$

The conformation of the protein in solution was determined using the GASBOR program from the ATSAS software package, which uses a chain of dummy residue centred at the Cα positions to represent the protein. A high-resolution structure (pdb:7OXF) was used to calculate the theoretical structure parameters.

For analysis with DENSS, the DENSSWeb server (https://denss.ccr.buffalo.edu) was used running 20 individual DENSS reconstructions and subsequent alignment and averaging.

All graphical representations were generated using PyMOL program (Schrödinger, L., & DeLano, W. (2020). *PyMOL*. Retrieved from http://www.pymol.org/pymol).

These reconstructions were performed inside the search volume of maximum dimension Dmax calculated from the p(r) determined for a set of measured scattering data by the GNOM program, which depicted an overall spherical object of 53 Å. The reconstructed models were obtained without imposing any restrictions on the symmetry and anisometry of the molecules and leaded to the expected spherical shell.

To treat samples with the magnetic field a 500-kHz sinusoidal signal was provided by a signal generator and applied through an amplifier to a 2500-turn solenoid coil (radius 2 cm) to produce an internal field strength of 50 mT. Samples were placed within the solenoid in an Eppendorf and treated for 60 min. The radiofrequency analysis has been performed in analogy to [19].

### 2.6. QCMD analysis

Quartz crystal microbalance with dissipation monitoring was performed at ILL-PSCM (Grenoble, FR) with a Q-Sense E4 instrument (Q-Sense, Biolin Scientific AB, Sweden), using $AlO_2$-coated 5 MHz quartz sensors. Crystals and O-rings were cleaned in an ultrasound bath with ethanol and ultrapure water, and then dried under a nitrogen flow.

Immediately before use, the crystals were treated with a UV ozone cleaner (BioForce Nanosciences, Inc., Ames, IA) for 15 min. As starting point, the fundamental frequency and the six overtones (3rd, 5th, 7th, 9th, 11th, and 13th) were recorded. The system was equilibrated in MQ water at 25 °C, until stable baselines were obtained. The samples were introduced in the flow cell at 0.1 mL/min and real-time shifts in the resonance frequencies (ΔFn) with respect to the calibration value were measured, with n representing the overtone number. The measured ΔFn is inversely proportional to the adsorbed mass on the sensor [37]. From the Sauerbrey equation the height of the sample can be evaluated, in our study assuming $\rho_{ferritin} = 1.35$ g/cm$^3$ and viscosity $\eta = 3.2$ mPa s:

$$h = \frac{\rho_0 h_0}{\rho \eta f_0} \frac{\Delta f}{n}$$

The permanent neodymium magnets used were either a ring magnet (26 mm width, 20 mm internal diameter, 2 mm height) or a bar magnet (5mm×5mm×20mm). Both magnets are axially magnetized (80 mT) and were purchased at Magfine Srl. For the magnet experiment, the magnet had a measured magnetic field of about 80mT.

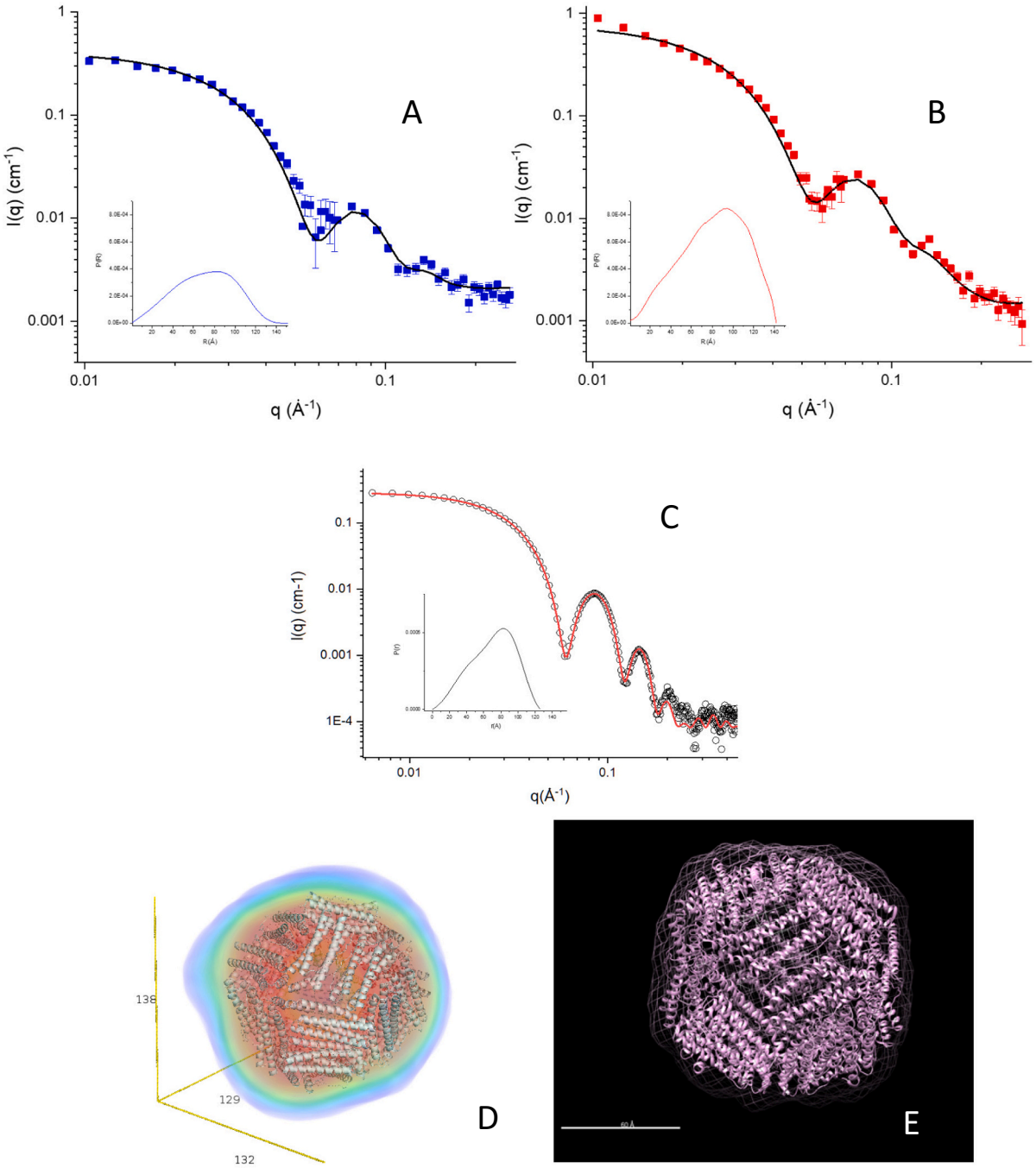


**Fig. 1.** Protein shell characterization of ferritins: A,B) SANS measurements of apo-.and holo-ferritins (respectively blue and red squares, 4.6 mg/mL) with best fitting reported in black solid lines. C) SAXS measurement of apo-ferritin in solution (4 mg/mL) with best fitting reported in red; D, E) SAXS reconstruction of apo-ferritin from SAXS data using Gasbor and Denss in comparison with the pdb structure (70HF). (For interpretation of the references to colour in this figure, the reader is referred to the web version of this article.)

## 3. Experimental results

With the aim to characterize the ferritin structure and its iron loading, we first studied the protein in two extreme conditions: the bare hollow protein, i.e. apo-ferritin, and the protein loaded with the maximum amount of iron, i.e. holo-ferritin. Further investigations were conducted to determine iron ions arrangement at different loading factors.

### 3.1. Purification and iron-loading of ferritins

The apo-ferritin structure self-assembles quite easily at room temperature at physiological pH and is stable in water for long times [32]. However, the presence of iron can promote protein aggregation in amorphous structures, given the propensity of iron to bridge unfolded monomers [33]. Thus, a crucial step prior to experimental analysis was the final purification step by HPLC performed on all samples to exclude aggregates. A preliminary check of particles by dynamic light scattering (DLS) technique certified the monodispersity of the samples after HPLC purification. In Fig. S1 the DLS results are shown, highlighting protein (apo and holo) monodispersity after purification by HPLC. Both proteins show a monodisperse distribution of particles with the expected dimension of about 10 nm. This procedure eliminates the population between 50 and 100 nm, as well as the higher size aggregates. Also, the stability of the protein structural arrangement over 4 months was checked, confirming the stable assembly of the particles, with and without iron, after this protocol.

### 3.2. Structure of ferritin: a protein shell

To gain insight into the protein conformation in solution and its iron loading, a combination of small angle scattering techniques (SAXS and SANS) was exploited.

SANS analysis on apo-ferritin and holo-ferritin was performed to assess the size and shape of the protein shell. Experimental SANS curves of apo and holo-ferritin, in $D_2O$ are reported in Fig. 1A and B. Additional measurements at 75 % $D_2O$ (25 % $H_2O$) were performed, making use of the contrast variation, and are reported in Supplementary materials (Fig. S2 and Table S2).

The scattering curves of both apo and holo-ferritin in solution display well-defined oscillations. Some differences in the profiles and intensities are visible, suggesting variations in the overall form factor between the apo and the holo-ferritin. The pair distribution functions (p(r)) of both SANS spectra are reported in the insets of Fig. 1A, B. The p(r) allowed to observe the protein overall features with model-free information about the size and shape of the macromolecules in solution. For both apo and holo-ferritin, asymmetric p(r) distributions were obtained, typical of hollow spheres [34]. A full characterization of the shape of the proteins was obtained by fitting the intensity profiles of the apo and the holo-ferritin with GENFIT software with core-shell models (as reported in Fig. 1A–B, black lines) [30]. Table 2 reports the fitting parameters considering a core shell sphere with a radius (R), a shell-thickness (T) and the respective scattering length densities for the apo-ferritin and holo-ferritin in $D_2O$, while the fitting curves and relative parameters of the proteins in $H_2O/D_2O$ (25 %:75 %) are reported in Fig. S2 and Table S2.

SANS apo-ferritin appeared as a hollow sphere, with core radius $R = 37$ Å and shell thickness $T = 29$ Å, as expected and in agreement with published data [35].

For the analysis of holo-ferritins it is worth noting that we obtained (see Table 1), a higher density of the inner core (from 6.35 $10^{10}$ $cm^{-2}$ to 6.88 $10^{10}$ $cm^{-2}$) indicating the effective presence of the iron inside the cage. Furthermore, the protein shape can be modelled both with a polydisperse core-shell sphere and a core-shell ellipsoid form factor with a 1.2 asymmetry of the internal cage (see Fig. S3). This result suggests a slight asymmetry of the particle when loaded up to saturation with iron.

Although it was not possible to carry out measurements with contrast matching of the protein, due to the high contribution of the incoherent scattering of $H_2O$, changing the contrast of the buffer allowed us to obtain more precise measurements of the protein shell, reducing uncertainties in the fitting parameters and increasing the signal-to-noise ratio. Moreover, if we consider that $D_2O$ approximatively matches the iron inside the core, lowering the contrast of the buffer can give us information on the permeation of the solvent inside the protein and the hydration of the iron in the core. Solvent exchange after iron loading from pure $D_2O$ to $H_2O/D_2O$ 25:75 revealed a slight lowering of the SLD of the inner core. This apparent low solvent penetration inside the cage of holo-ferritin suggests that the internal volume is mostly occupied by iron.

Parallel SAXS analysis was performed on apo-ferritin to determine the protein shell. The scattering profile (Fig. 1C), showed well-defined features similar to the ones already observed in both SANS profiles, and the p(r) distribution, reported in inset, is asymmetric, as expected for a hollow sphere. The 3D structure of apo-ferritin was easily reconstructed (Fig. 1D and E) and compared with the literature PDB [31,36]. The full analysis of the SAXS data was carried out, analogously to SANS, by fitting the scattering curve with a form factor of a core-shell sphere. The fitting curve is reported in Fig. 1C (red line) and the parameters in Table 3. The overall radius of the protein (62 Å) and the inner radius of the core (36 Å) are in accordance with the SANS parameters. Results show that apo-ferritin assembles into a hollow sphere, which deforms slightly into an ellipsoid when loaded to saturation with iron.

### 3.3. Iron disposition at different loading factors

We analysed the ferritins with increasing iron amounts. Fig. 2A displays SAXS data for ferritin samples at different iron loading factors, from the apo-ferritin towards holo-ferritin showing intensity profiles with different features, that suggest the transition from a hollow spherical cage to an iron loaded protein. By increasing the amount of iron incorporated into apo-ferritin, the troughs between maxima shallow gradually. Also, the first minimum is shifted towards higher q (from approximately 0.06 to 0.1 $Å^{-1}$). It is clearly visible that the 500 Fe/Ft curve represents a turning point, conserving some features of the apo-ferritin profile, but also showing additional features, similar to the ones of the high loading factors (LF) curves. The changes in the SAXS spectra reflect in the calculated p(r) distributions (Fig. 2B). The increase in the amount of iron inside the protein core leads to a shift from a characteristic core shell distribution, asymmetric towards high radius values [34], to an asymmetric distribution towards low radius values, the turning point being 500 Fe/Ft. This shift can be linked to the progressive increase of the scattering contribution of the inner core with respect to the one of the external protein shells. The increase in the total scattered intensity, evident in both representations and estimated in Fig. S4 by means of a Gaussian fitting, is also strictly linked to the increase in contrast due to the iron presence. At high loading factors, the scattering intensity contribution of the iron is exceeding with respect to the one of the proteins; the spectra are mostly modulated by the shape of the inner

**Table 2**
Fitting parameters from a core shell sphere model for SANS measurements of apo-ferritin and holo-ferritin. SLD of $D_2O$ and protein shell were kept constant.

| | R (Å) | T (Å) | Rtot (Å) | SLD core ($10^{10}$ $cm^{-2}$) | SLD shell ($10^{10}$ $cm^{-2}$) | PDI radius | $X^2$ |
|---|---|---|---|---|---|---|---|
| Apo-ferritin | 37 ± 2 | 29 ± 2 | 66 ± 4 | 6.35 | 2.3 | 0.10 ± 0.05 | 0.1 |
| Holo-ferritin | 40 ± 2 | 26 ± 2 | 66 ± 4 | 6.88 ± 0.3 | 2.3 | 0.15 ± 0.05 | 0.2 |

**Table 3**
Fitting parameters for SAXS measurements of ferritins at different iron content (Fe/Ft). A spherical core multi-shell model and a tri-axial ellipsoidal core multi-shell model were used. The protein and the water SLD were kept constant.

| Model | Parameters | Iron loading | | | | | | |
|---|---|---|---|---|---|---|---|---|
| | Fe/Ft | **0** | **50** | **150** | **500** | **1000** | **2000** | **Saturation** |
| Spherical core-shell | $R_{core}$ (Å) | 36 ± 1 | 36 ± 1 | 18 ± 1 | 20 ± 1 | – | – | – |
| | $T_{internal\ shell}$ (Å) | – | – | 22 ± 1 | 22 ± 1 | – | – | – |
| | $T_{external\ shell}$ (Å) | 26 ± 1 | 25 ± 1 | 21 ± 1 | 20 ± 2 | – | – | – |
| | $SLD_{core}(10^{10}\ cm^{-2})$ | 9.3 | 9.58 ± 0.03 | 10.4 ± 0.1 | 10.1 ± 0.1 | – | – | – |
| | $SLD_{internalshell}(10^{10}\ cm^{-2})$ | – | – | 9.58 ± 0.03 | 9.35 | – | – | – |
| | $SLD_{externalshell}(10^{10}\ cm^{-2})$ | 12.3 | 12.3 | 12.3 | 12.4 ± 0.1 | – | – | – |
| Ellipsoidal core-shell | double axis | – | – | – | 21 ± 1 | 21 ± 1 | 23 ± 1 | 22 ± 1 |
| | single axis | – | – | – | 36 ± 1 | 37 ± 1 | 38 ± 1 | 35 ± 1 |
| | $T_{internal\ shell}$ (Å) | – | – | – | 18.7 ± 0.5 | 15.0 ± 0.5 | 15.2 ± 0.5 | 15.0 ± 0.5 |
| | $T_{external\ shell}$ (Å) | – | – | – | 17.5 ± 0.5 | 20 ± 0.5 | 19.4 ± 0.5 | 16.5 ± 0.5 |
| | $SLD_{core}(10^{10}\ cm^{-2})$ | – | – | – | 32.7 ± 0.5 | 35.5 ± 0.5 | 38.0 ± 0.5 | 40.0 ± 0.5 |
| | $SLD_{internalshell}(10^{10}\ cm^{-2})$ | – | – | – | 9.3 | 9.3 | 9.3 | 9.3 |
| | $SLD_{externalshell}(10^{10}\ cm^{-2})$ | – | – | – | 12.4 ± 0.1 | 12.4 | 12.4 | 12.4 |
| | $\chi^2$ | 1.3 | 0.2 | 1.5 | 0.7 | 1.6 | 1.7 | 0.41 |

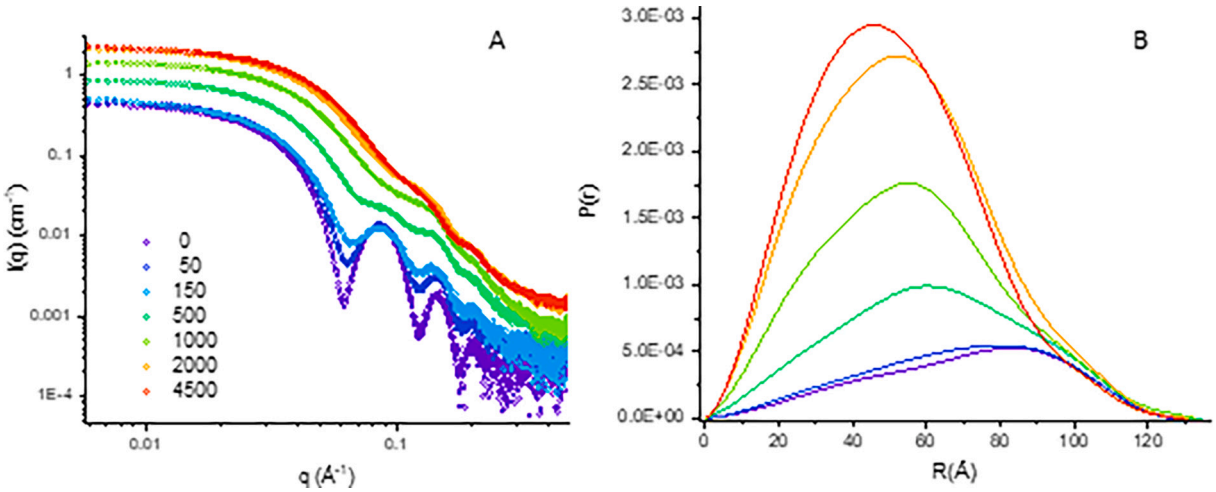


**Fig. 2.** A) SAXS curve for apo-ferritin (4 mg/mL) and B) related p(r) distribution (ID02, ESRF).

core of ferritin rather than by the external protein shell.

The detailed form factors of the samples at increasing iron content have been assessed by fitting the data with GENFIT software. Fig. 3 reports the best fit to the data with the parameters and the models used reported in Table 3.

For the curves with a low iron content a spherical core-shell model was still considered, including a homogeneous, iron-oxide-containing core surrounded by a protein shell and a constant low polydispersity (0.1). At 50 Fe/Ft, the overall size of the protein was kept constant ($R$ = 61 Å), while a slight increase in the scattering length density of the inner core is visible, from 9.3 to 9.58 $10^{10}$ $cm^{-2}$. The uniform density of the core suggests a homogeneous iron arrangement inside the protein. This result indicates that, when encapsulated in low amount inside the cage, the iron is not arranged in a solid defined form. It is rather dispersed in the aqueous solution. Roughly considering the SLD of the iron, the data account for 45 Fe/Ft, in good agreement with the nominal amount of iron disposable for each ferritin.

Interestingly, the intensity profile of ferritin at higher iron content (namely 150 Fe/Ft) could no longer be fitted with a core-shell sphere model with a homogeneous SLD (9.58 $10^{10}$ $cm^{-2}$) for the inner core. A good fitting solution was obtained using a three-density level sphere: the innermost has a size $R$ = 18 Å and a high SLD = 10.4 $10^{10}$ $cm^{-2}$, surrounded by an intermediate shell (thickness 22 Å) with SLD = 9.58 $10^{10}$ $cm^{-2}$ and by the protein shell. These results indicate the formation of a defined core of iron inside the protein cage. The ions seem to coalesce to reach a defined arrangement and to cluster at the centre of the protein cage.

At 500 Fe/Ft iron content, the coexistence of two form factors should be accounted to reach a good fitting solution. In addition to the spherical core-shell model, a second form factor representing an ellipsoidal core shell was needed. The coexistence of two populations (66 % spheres, 33 % ellipsoid) was considered to reconstruct the experimental curve. Spheres fit parameters are similar to the one exploited for the previous LF sample (with a central denser core, $R$ = 20 Å, SLD = 10.1 $10^{10}$ $cm^{-2}$). The core-shell prolate ellipsoid shows instead an innermost core with internal asymmetry of 1.7 (axial ratio) and very high SLD (32.7 $10^{10}$ $cm^{-2}$) surrounded by an aqueous shell (thickness 18.7 Å) and by the protein shell. After this critical point, the SAXS curves could be analysed using only the form factor of a three-axial core-shell ellipsoid. The inner ellipsoid increased in size with the iron content, preserving the asymmetry (inner core axial ratio 1.7, external axial ratio 1.3). The overall size of the protein was also kept constant. Results indicate that in the presence of greater quantities of available iron, the iron continues to accumulate in asymmetric clusters increasing in size in the internal cavity of ferritin. The SAXS scattering length density of the core evolves towards higher values reaching the one, expected, of ferrihydrite (35•$10^{10}$ $cm^{-2}$) at 1000 Fe/Ft and overtaking it, achieving the value typical of magnetite (40•$10^{10}$ $cm^{-2}$) in holo-ferritin form.

The ab-initio reconstruction of Fe/Ft proteins at different loadings, reported in Figs. 3 and S5, are in agreement with the shapes obtained by fitting, confirming the non-spherical arrangement of the protein at higher iron loadings. Fig. 4 summarizes in a sketch the loading

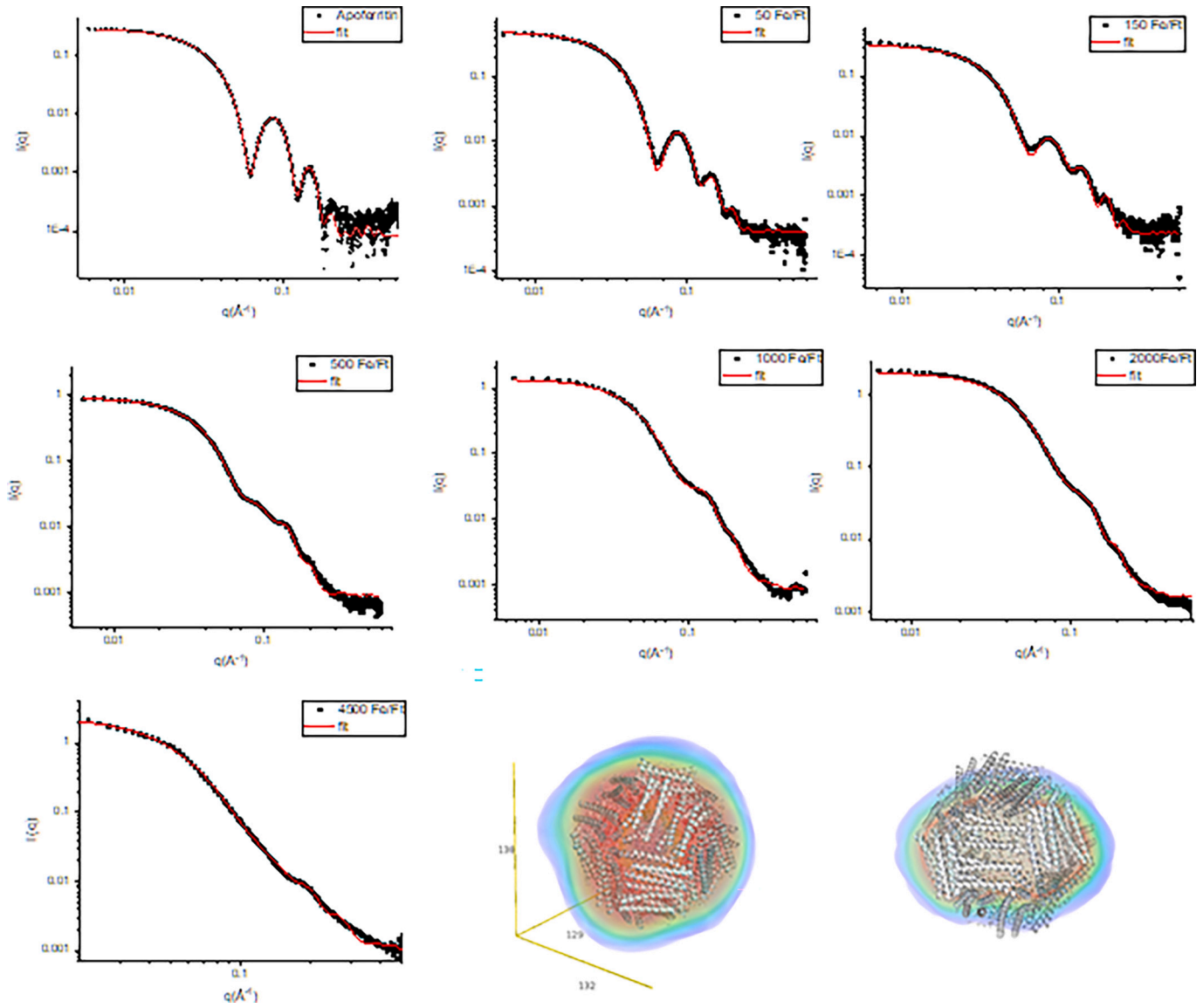


**Fig. 3.** Data and fitting of SAXS curves for ferritin (4 mg/mL) at different loading factors. Ab initio SAXS derived envelopes for apo-ferritin and holo-ferritin compared with PDB structure (pdb:7OXF). In Fig. S5 the reconstruction of the different LF ferritins is reported.

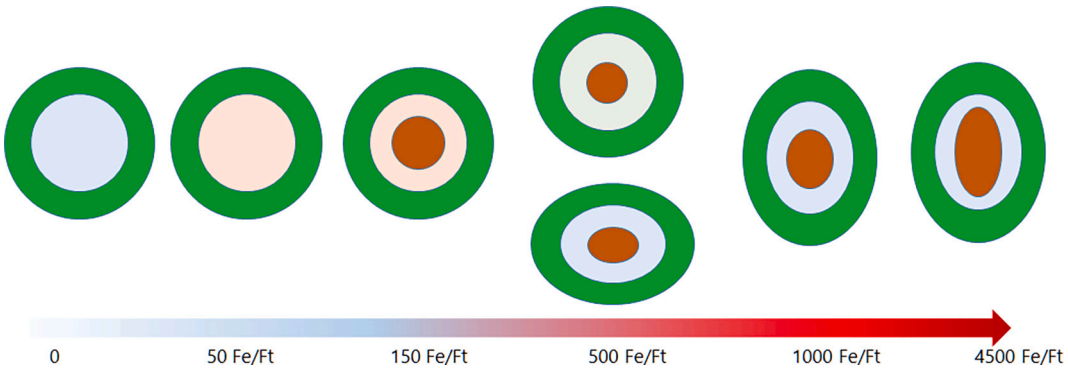


**Fig. 4.** sketch of ferritins at increasing iron loading. The asymmetry of the core shell ellipsoid is exaggerated for better underlining the differences.

progression, to better visualize the evolution of the protein arrangement at increasing iron concentrations. It is interesting to note that, with the loading procedure used, a uniform loading of the ferritins can be achieved: at each given iron amount dispersed in the apo-ferritin solution, an equilibrium condition is reached, where a uniform distribution of iron among the proteins and a defined arrangement of the ions in the protein cage is observed. Instead of a polydisperse population, depending on the spontaneous loading of each protein in respect to

another, the pool arranges itself in mostly the same way internalizing the same amount of iron. The only exception is the peculiar case of 500 Fe/Ft, which shows a bimodal distribution. This stable configuration seems to represent a pivotal point between the spherical arrangement and the ellipsoidal arrangement.

Experimental results show that at low concentrations of iron, the atoms are dispersed homogeneously inside the core. This disposition could correlate with the functional role of ferritin, which can promptly respond to changes in the iron requirement of the external environment. The increase in iron content leads to the formation of a structured core. Interestingly, the protein spherical cage is able to deform in a prolate ellipsoidal cage, allowing to encapsulate a huge amount of iron, clustered in a central elongated crystalline core. This core is separated from the internal surface of the protein shell by a thin layer of water. The protein cage seems to direct the formation of crystalline clusters of iron with increasing compactness. The overall behaviour can correlate with the main functional role of ferritin, as an efficient iron saver and regulator and reveals the extraordinary ability of ferritin to encapsulate very high quantities of iron thanks to its modular structure which probably makes its ensemble both stable and deformable.

### 3.4. Ferritins' interaction with a magnetic field

The structural results on ferritin at different loading factors support the possibility to use the loaded ferritin as a biomaterial for magnetic applications. For this purpose, we tested the protein's response to static and oscillating magnetic field, when loaded with different amounts of iron.

A first study of the proteins' response to a static magnetic field was conducted by QCM-D analysis, observing the rearrangement, if any, of the holo-ferritins deposited onto a resonant $AlO_2$ sensor after the addition of a static magnetic field. The inset of Fig. 5 reports the deposition of the ferritins on the active surface. It can be observed that the protein layer on $Al_2O_3$ is thick and stable, as the different overtones overlay nicely. Again, from the Sauerbrey equation, assuming the viscosity and density of the protein as in the average, the thickness of the layer can be determined, that is 10.7±0.2 nm, indicating a single layer of proteins.

The holo-ferritin response to a static magnetic field of 80 mT is represented by a subtle variation mostly in the third overtone. This change in the deposition is stable after removing and again adding the magnet. This indicates that the magnetic particles rearrange to form a more compact and stable layer on the surface (Fig. 5), as demonstrated by the apparent addition of mass. Also, the asymmetry of the particle is further confirmed, since the reorientation of a magnetic core should not influence the thickness and compactness of the deposition if the particle was spherical.

By means of SAXS technique also information on the effect induced by a RF magnetic field on the ferritin solutions at different loading factors could be observed. The protein samples were treated with a radiofrequency (RF) magnetic field for 1 h and then measured to observe structural reorganizations of the core, if any. Interestingly, no modifications were noted for samples at high LFs, as reported in Fig. S6. Instead, a slight modification can be detected in the 150 Fe/Ft curve (Fig. 6). The differences between the original sample and the one after RF treatment are mainly in the depth of intensity minima, suggesting a more homogeneous contrast of the internal core of the protein after the perturbation as observed in samples with lower LF. The fitting parameters of the new configuration are reported in Table 4. Notably, the effect of RF switches the system towards a condition in which iron is diffused inside the core without creating a crystal. The iron in the centre is thus more available rather than more structured. It is also interesting to note that since the RF treatment was conducted 48 h before the measurements, the condition observed is stable: once disrupted, the crystalline core is not able to reform over days. For the higher loading factors, no modifications were detected, because of the stability of the iron cluster or the ability of the systems to recover the initial configuration before the measurements.

## 4. Discussion

The stability of the protein, its easiness of production, the unique structure, and its suitability for bioengineering applications kept ferritin in the limelight until present days. Here we analysed the ferritin in its apo form, that is without any content, and in presence of different amounts of iron, up to the holo-ferritin, in which the protein is filled with the maximum amount of iron achievable. Thanks to the combined

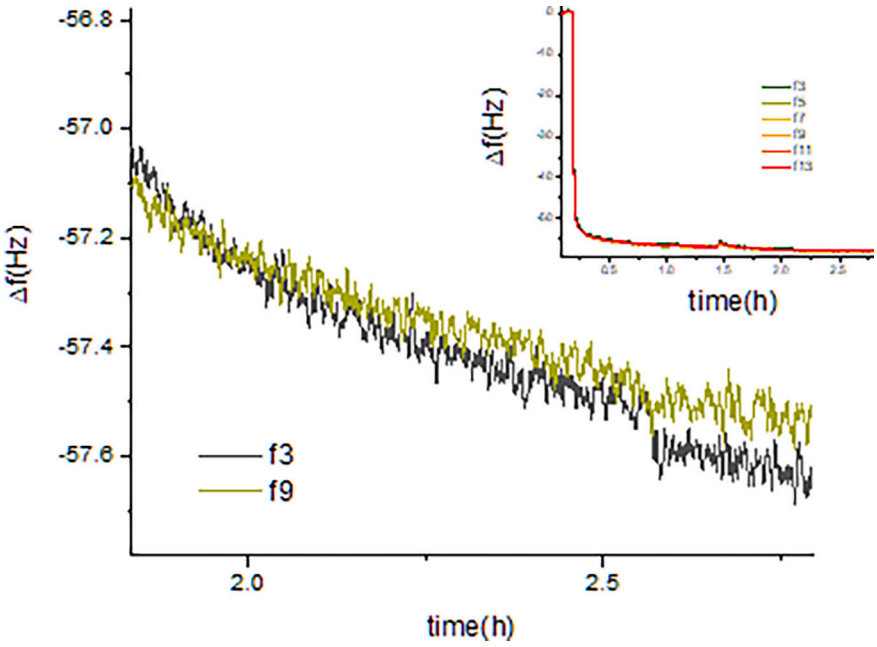


**Fig. 5.** QCM-D. Frequency modifications observed for holo-ferritin after the application of a static magnetic field: overtone 3 (light green) and 9 (dark green). In the inset the frequency changes upon deposition of ferritins (1 mg/mL) on the alumina surface at different overtones. (For interpretation of the references to colour in this figure legend, the reader is referred to the web version of this article.)

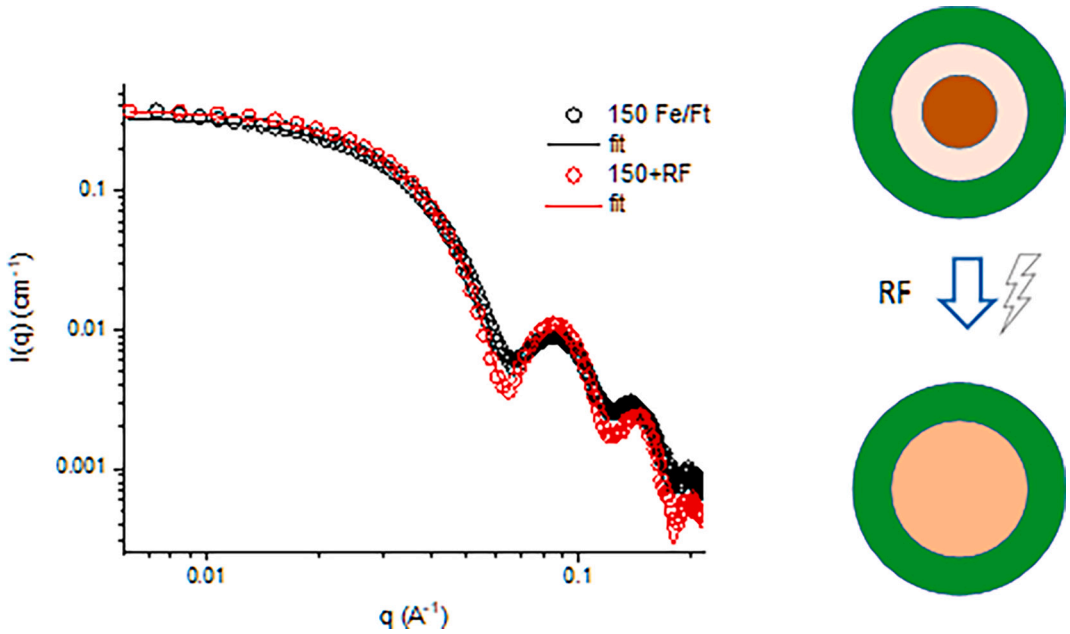


**Fig. 6.** RF effect on iron loaded ferritins: left) SAXS curves of ferritin at 150 Fe/Ft before (black circles) and after (red circles) the treatment with RF, with the respective fits (solid lines). Right: sketch of RF effect on loaded ferritins. (For interpretation of the references to colour in this figure legend, the reader is referred to the web version of this article.)

**Table 4**
Fitting parameters of SAXS data before and after RF application. Protein and solvent SLD were kept constant.

| Parameters | $R_{core}$ (Å) | $T_{internalshell}$ (Å) | $T_{externalshell}$ (Å) | $R_{tot}$ (Å) | $SLD_{core}$ ($10^{10}$ $cm^{-2}$) | $SLD_{internalshell}$ ($10^{10}$ $cm^{-2}$) | $SLD_{externalshell}$ ($10^{10}$ $cm^{-2}$) | Fe/Ft | PD | $\chi^2$ |
|---|---|---|---|---|---|---|---|---|---|---|
| 150 Fe/Ft | 18 ± 1 | 22 ± 1 | 21 ± 1 | 61 ± 3 | 10.4 ± 0.2 | 9.6 ± 0.1 | 12.3 | 178 | 0.10 ± 0.04 | 1.5 |
| 150 Fe/Ft + RF | 41 ± 2 | – | 20 ± 1 | 61 ± 3 | 9.7 ± 0.3 | – | 12.3 | 190 | 0.10 ± 0.05 | 1.3 |

use of different scattering techniques, we could determine the overall and internal structure of the protein. The core-shell structure of the protein was determined by SANS, which visualized the protein shell in the apo and holo-ferritin. Complementary SAXS experiments allowed describing the shape of the protein and the arrangement of different amounts of iron loaded inside the protein cage, ranging from 50 atoms for ferritin to saturation.

It is known that metal nanoparticles in protein scaffolds are formed by incorporation of ions, followed by nucleation, which leads to the formation of a small sub-nanocluster as metal core [38]. Our structural results show that at low iron concentrations, all the ions enter the ferritin cage but remain dispersed in solution. In this way they are free to move inside a pool and are more available for extrusion, if required for external homeostasis. Increasing the amount of iron, up to a critical iron concentration, favours the formation of a crystalline nanocluster. We could infer the amount of iron needed for the transition from diffuse to organized iron, about 150 Fe/Ft, since the X-ray scattering length density, until the formation of crystals inside the protein, nicely corresponds to an iron pool where the number of iron atoms is compatible with the expected uptake, i.e. all the ions which are available at each sample. The formation of iron-oxo particles inside these compartments fulfils two aims: the rapid uptake, oxidation, and storage of free iron effectively protects the cells from the Fenton reaction and the formation of particles precisely controls the storage and mobilization of iron to maintain the homeostasis at high iron contents. In this high iron content regime, we found by both scattering techniques a scattering length density of the crystalline inner core slightly higher ($40\bullet10^{10}$ $cm^{-2}$ and $6.8\bullet10^{10}$ $cm^{-2}$ for SAXS and SANS respectively) than the one of ferrihydrite ($35\bullet10^{10}$ $cm^{-2}$ for SAXS and $6.5\bullet10^{10}$ $cm^{-2}$ for SANS), reported to be the main crystalline phase in the literature.

Our result can have different explanations. It is known that the inner core of the high LF ferritin is mainly composed of ferrihydrite, with hexagonal unit cell [39]. A ferrihydrite with higher density of iron was reported in Michel model, in which a 20 % of $FeO_4$ was observed [40]. The effectiveness of this arrangement has been the subject of considerable debate [41,42].

Still, since the SAXS scattering length density of the core reaches a value more similar to the one of magnetite ($40\bullet10^{10}$ $cm^{-2}$ and $7\bullet10^{10}$ $cm^{-2}$ for SAXS and SANS) the prevalent presence of this crystal, with higher iron content, can be hypothesized. It has been reported that the core of AD pathological ferritin, for example, consists primarily of magnetite and wustite, and to a lesser extent of ferrihydrite [43]. It can be supposed that the iron loading procedure, being in vitro, can lead to a clustering of iron in a different form, that is the one of magnetite.

Interestingly the iron accumulation proves to be an ordered process, leading for each sample to a uniform population of iron arranged in the same way inside each protein cage. The asymmetry of the mineral core, that can be expected if we assume the growth of a crystal inside the protein, intrinsically arranging in a non-spherical shape, confirms the plasticity of the protein shell. Thanks to its modular, assemblable structure which makes the protein deformable and adaptable, ferritins are able to encapsulate very high quantities of iron that can arrange in different ways, therefore allowing efficient iron gathering and regulation.

The slight disproportion of the high LF proteins draws attention to magnetic applications of the ferritins. The magnetic field effect, tested with the QCM-D analysis, effectively provokes a reorientation of the proteins, that could not be seen if the proteins were perfect spheres.

Given the sensitivity of the technique we detected the reorientation only in the sample with the maximum amount of iron, but the characterization of an asymmetric inner core may suggest an effect for all the particles with a ferric crystallised core.

Recently it has been attempted to use ferritin as a sensor component for the magnetic field in an ion channel protein. The fusion of ferritin to the channel should allow channel gating by the response of the ferritin molecule in the magnetic field. In proof of concept experiments it was shown that a coupling of ferritin to the cytosolic domain of the TRPV1 channel was indeed able to gate this channel remotely by a radiofrequency magnetic field [19,20]. While these results show that ferritin-tethered ion channels can be gated by magnetic fields, the underlying mechanism remains unclear, and hypothesis include local temperature increase, mechanic displacement of the channel or the effect of localized induced electric fields [22,44]. Recent works suggest that the generation of reactive oxygen species (ROS) linked to the extroflection of iron can have an effect on the TRPV1 downstream signalling [45,46]. In this study we could observe an effect of RF magnetic field on iron loaded ferritins by means of SAXS technique. Contrary to what one might expect, we could detect this effect only in one of the samples with low iron content (150 Fe/Ft). The protein shows an inner crystallised core surrounded by a less dense iron-water buffer, encapsulated inside the protein shell. The arrangement of iron is thus in a transition state, from the iron dispersed pool inside the ferritin towards the crystallised central core. The application of a magnetic RF field for 1 h presumably dissolves the iron central core of the protein, leading to an arrangement in which iron is dispersed inside the protein cage. The new RF-induced arrangement of iron is stable, for at least 48 h after the RF application. This effect is undetectable in other LFs proteins. However, in samples with very low LF the distribution of iron is already homogeneous, while the case of high LF, on the other hand, could be biased intrinsically by the fact that iron is contained in such large amounts that it is difficult for the RF to disrupt the core. A certain amount of iron could detach from the crystallised core, but it would be barely visible by SAXS in presence the structured crystal. The transition towards a more dispersed state of iron inside the ferritin core can imply some energy exchange during the magnetic field application that can affect the nearby molecules and reflect in a higher availability of iron that can promptly exit the protein cage, in a cellular environment. The coexistence of free iron ions and iron oxide crystals makes the 150 Fe/Ft sample an edge case that can be modified dramatically and irreversibly by the application of the radiofrequency magnetic field. Although this result presents experimental limitations, it indicates an actual modification of the iron organization inside the protein in presence of a RF magnetic field with an intensity similar to the one activating the TRPV1 channel [19,20]. This preliminary result offers a glimpse into the mechanism underlying the magnetic-driven ion channel activation and opens to the possibility of exploiting constructs with ferritin for magnetogenetic applications.

## 5. Conclusions

The study provides insights into the structural dynamics of ferritin under varying iron concentrations and the effects of an RF magnetic field. By utilizing combined scattering techniques, the research reveals both the overall and internal structure of ferritin in its apo form and when loaded with different amounts of iron. At low iron concentrations, the ions remain dispersed within the ferritin cage, allowing for rapid mobilization by external stimuli. As the iron concentration increases, there is a transition from a dispersed state to the formation of crystalline nanoclusters. This process highlights ferritin's role in iron homeostasis, where the formation of iron-oxo particles helps in the rapid uptake and storage of iron, thereby protecting cells from oxidative damage. The study identifies that this transition to an ordered iron arrangement occurs at approximately 150 Fe/Ft, indicating a balance between iron availability and storage efficiency. In conditions of high iron content, the crystalline core within ferritin exhibits higher scattering length densities, suggesting the presence of denser iron forms, such as magnetite, particularly in in vitro conditions.

Notably, ferritins loaded with a moderate amount of iron (150 Fe/Ft) showed significant structural changes when exposed to an RF magnetic field. This reorganization under the RF magnetic field provides insights on the mechanisms of gating in a ferritin coupled ion channel when a radiofrequency magnetic field is applied. This information can give new details for bioengineering exploitation of ferritins, especially in the activation of ion channels like TRPV1 through remote gating strategies.

## CRediT authorship contribution statement

**Caterina Ricci:** Writing – review & editing, Writing – original draft, Investigation, Formal analysis, Conceptualization. **Gerardo Abbandonato:** Investigation, Formal analysis. **Matteo Giannangeli:** Investigation, Formal analysis. **Lauren Matthews:** Investigation, Formal analysis. **László Almásy:** Investigation, Formal analysis. **Barbara Sartori:** Investigation, Formal analysis. **Alessandro Caselli:** Writing – review & editing, Methodology. **Alberto Boffi:** Writing – review & editing, Methodology. **Gerhard Thiel:** Writing – review & editing, Methodology, Conceptualization. **Elena Del Favero:** Writing – review & editing, Writing – original draft, Methodology, Conceptualization. **Anna Moroni:** Writing – review & editing, Writing – original draft, Methodology, Conceptualization.

## Declaration of competing interest

The authors declare that they have no known competing financial interests or personal relationships that could have appeared to influence the work reported in this paper.

## Acknowledgments

The authors acknowledge the ESRF, ID02 beamline (10.15151/ESRF-ES-281427365), Elettra, Budapest Neutron Center for financial and technical assistance. The authors thank ILL PSCM for provision of QCMD facility and the staff for assistance and support. The authors thank Eugenio Tarolli Bramè for SAXS experiments and Laura Cantù for her scientific contribution. This work was supported by ERC Grant (ID:695078, H2020-EU.1.1. – EXCELLENT SCIENCE – European Research Council (ERC)).

## References

[1] E.C. Theil, D.J. Goss, Living with iron (and oxygen): questions and answers about iron homeostasis, Chem. Rev. (2009), https://doi.org/10.1021/cr900052g.
[2] S.J. and T. Price, Living with iron and oxygen, Bone 23 (2008) 1–7, https://doi.org/10.1021/cr900052g.Living.
[3] L. Bai, T. Xie, Q. Hu, C. Deng, R. Zheng, W. Chen, Genome-wide comparison of ferritin family from archaea, bacteria, eukarya, and viruses: its distribution, characteristic motif, and phylogenetic relationship, Sci. Nat. 102 (2015), https://doi.org/10.1007/s00114-015-1314-3.
[4] P. Arosio, L. Elia, M. Poli, Critical review ferritin, cellular iron storage and regulation, IUBMB Life 6 (2017) 414–422, https://doi.org/10.1002/iub.1621.
[5] S. Levi, P. Santambrogio, B. Corsi, A. Cozzi, P. Arosio, Evidence that Residues Exposed on the Three-Fold Channels Have Active Rolesin the Mechanism of Ferritin Iron Incorporation 473, 1996, pp. 467–473.
[6] P. Chen, E. De Meulenaere, D.D. Deheyn, P.R. Bandaru, Iron redox pathway revealed in ferritin via electron transfer analysis, Sci. Rep. 10 (2020) 1–10, https://doi.org/10.1038/s41598-020-60640-z.
[7] C. Pozzi, F. Di Pisa, C. Bernacchioni, S. Ciambellotti, P. Turano, S. Mangani, Iron binding to human heavy-chain ferritin, Acta Crystallogr. D Biol. Crystallogr. 71 (2015) 1909–1920, https://doi.org/10.1107/S1399004715013073.
[8] N.D. Chasteen, P.M. Harrison, Mineralization in ferritin: an efficient means of iron storage, J. Struct. Biol. 126 (1999) 182–194, https://doi.org/10.1006/jsbi.1999.4118.
[9] G. Jutz, P. Van Rijn, B. Santos Miranda, A. Böker, Ferritin: a versatile building block for bionanotechnology, Chem. Rev. (2015), https://doi.org/10.1021/cr400011b.
[10] W.R. Hagen, P.L. Hagedoorn, K. Honarmand Ebrahimi, The workings of ferritin: a crossroad of opinions, Metallomics 9 (2017) 595–605, https://doi.org/10.1039/c7mt00124j.

[11] W.R. Hagen, Maximum iron loading of ferritin: half a century of sustained citation distortion, Metallomics 14 (9) (2022) mfac063, https://doi.org/10.1093/mtomcs/mfac063.
[12] K.H. Ebrahimi, P.L. Hagedoorn, L. Van Der Weel, P.D.E.M. Verhaert, W.R. Hagen, A novel mechanism of iron-core formation by Pyrococcus furiosus archaeoferritin, a member of an uncharacterized branch of the ferritin-like superfamily, J. Biol. Inorg. Chem. 17 (2012) 975–985, https://doi.org/10.1007/s00775-012-0913-0.
[13] B. Maity, S. Abe, T. Ueno, Observation of gold sub-nanocluster nucleation within a crystalline protein cage, Nat. Commun. 8 (2017), https://doi.org/10.1038/ncomms14820.
[14] M. Truffi, L. Fiandra, L. Sorrentino, M. Monieri, F. Corsi, S. Mazzucchelli, Ferritin nanocages: a biological platform for drug delivery, imaging and theranostics in cancer, Pharmacol. Res. 107 (2016) 57–65, https://doi.org/10.1016/j.phrs.2016.03.002.
[15] C. Zhang, X. Zhang, G. Zhao, Ferritin nanocage: a versatile nanocarrier utilized in the field of food, nutrition, and medicine, Nanomaterials 10 (2020) 1–25, https://doi.org/10.3390/nano10091894.
[16] D.M. Monti, G. Ferraro, A. Merlino, Ferritin-based anticancer metallodrug delivery: crystallographic, analytical and cytotoxicity studies, Nanomedicine 20 (2019) 101997, https://doi.org/10.1016/j.nano.2019.04.001.
[17] L. Affatigato, M. Licciardi, A. Bonamore, A. Martorana, A. Incocciati, A. Boffi, V. Militello, Ferritin-coated SPIONs as new cancer cell targeted magnetic nanocarrier, Molecules 28 (2023) 1163, https://doi.org/10.3390/molecules28031163.
[18] C. Quintana, S. Bellefqih, J.Y. Laval, J.L. Guerquin-Kern, T.D. Wu, J. Avila, I. Ferrer, R. Arranz, C. Patiño, Study of the localization of iron, ferritin, and hemosiderin in Alzheimer's disease hippocampus by analytical microscopy at the subcellular level, J. Struct. Biol. 153 (2006) 42–54, https://doi.org/10.1016/j.jsb.2005.11.001.
[19] S.A. Stanley, J. Sauer, R.S. Kane, J.S. Dordick, J.M. Friedman, Remote regulation of glucose homeostasis in mice using genetically encoded nanoparticles, Nat. Med. 21 (2015) 92–98, https://doi.org/10.1038/nm.3730.
[20] U. Sauer, A. Schicker, J. Tyerman, M. Bertrand, M. Doebeli, M. Travisano, E. Fischer, J.L. Reed, B.O. Palsson, R. Smith, M.A. Eiteman, E. Altman, M. Diseases, J.A. Papin, I. Thiele, L. Kuepfer, C.D. Maranas, D. Vitkup, G.M. Church, Radio-wave heating of iron oxide, Science 336 (2012) (1979) 604–608.
[21] M. Meister, Physical limits to magnetogenetics, Elife 5 (2016) 1–14, https://doi.org/10.7554/eLife.17210.
[22] M. Barbic, Possible magneto-mechanical and magneto-thermal mechanisms of ion channel activation in magnetogenetics, Elife 8 (2019) 1–18, https://doi.org/10.7554/eLife.45807.
[23] P. Lago, L. Rovati, L. Cantù, M. Corti, A quasielastic light scattering detector for chromatographic analysis, Rev. Sci. Instrum. 64 (1993) 1797–1802, https://doi.org/10.1063/1.1144013.
[24] C.I. Camara, L. Bertocchi, C. Ricci, R. Bassi, A. Bianchera, L. Cantú, R. Bettini, E. Del Favero, Hyaluronic acid—dexamethasone nanoparticles for local adjunct therapy of lung inflammation, Int. J. Mol. Sci. 22 (2021), https://doi.org/10.3390/ijms221910480.
[25] P. Andreozzi, C. Ricci, J.E.M. Porcel, P. Moretti, D. Di Silvio, H. Amenitsch, M. G. Ortore, S.E. Moya, Mechanistic study of the nucleation and conformational changes of polyamines in presence of phosphate ions, J. Colloid Interface Sci. 543 (2019) 335–342, https://doi.org/10.1016/j.jcis.2019.02.040.
[26] A.V. Nagornyi, V. Socoliuc, V.I. Petrenko, L. Almasy, O.I. Ivankov, M.V. Avdeev, L. A. Bulavin, L. Vekas, Structural characterization of concentrated aqueous ferrofluids, J. Magn. Magn. Mater. 501 (2020), https://doi.org/10.1016/j.jmmm.2020.166445.
[27] N. Theyencheri, et al., Performance of the time-resolved ultra-small-angle X-ray scattering beamline with the Extremely Brilliant Source, J. Appl. Crystallogr. 55 (1) (2022) 98–111, https://doi.org/10.1107/S1600576721012693.
[28] H. Amenitsch, M. Rappolt, M. Kriechbaum, H. Mio, P. Laggner, S. Bernstorff, First performance assessment of the small-angle X-ray scattering beamline at ELETTRA, J. Synchrotron Radiat. 5 (1998) 506–508, https://doi.org/10.1107/S090904959800137X.
[29] L. Almásy, New measurement control software on the yellow submarine SANS instrument at the Budapest Neutron Centre, J. Surf. Invest. 15 (2021) 527–531, https://doi.org/10.1134/S1027451021030046.
[30] F. Spinozzi, C. Ferrero, M.G. Ortore, A. De Maria Antolinos, P. Mariani, GENFIT: software for the analysis of small-angle X-ray and neutron scattering data of macromolecules in solution, J. Appl. Cryst. 47 (2014) 1132–1139, https://doi.org/10.1107/S1600576714005147.
[31] D.I. Svergun, M.V. Petoukhov, M.H.J. Koch, Determination of domain structure of proteins from x-ray solution scattering, Biophys. J. (2001), https://doi.org/10.1016/S0006-3495(01)76260-1.
[32] J. Tatur, W.R. Hagen, P.M. Matias, Crystal structure of the ferritin from the hyperthermophilic archaeal anaerobe Pyrococcus furiosus, J. Biol. Inorg. Chem. 12 (2007) 615–630, https://doi.org/10.1007/s00775-007-0212-3.
[33] K. Joppe, A.E. Roser, F. Maass, P. Lingor, The contribution of iron to protein aggregation disorders in the central nervous system, Front. Neurosci. 13 (2019) 1–11, https://doi.org/10.3389/fnins.2019.00015.
[34] D.I. Svergun, M.H.J. Koch, Small-angle scattering studies of biological macromolecules in solution, Rep. Prog. Phys. 66 (2003) 1735–1782, https://doi.org/10.1088/0034-4885/66/10/R05.
[35] L. Melníková, V.I. Petrenko, M.V. Avdeev, V.M. Garamus, L. Almásy, O.I. Ivankov, L.A. Bulavin, Z. Mitróová, P. Kopčanský, Effect of iron oxide loading on magnetoferritin structure in solution as revealed by SAXS and SANS, Colloids Surf. B Biointerfaces 123 (2014) 82–88, https://doi.org/10.1016/j.colsurfb.2014.08.032.
[36] T.D. Grant, Ab initio electron density determination directly from solution scattering data, Nat. Methods 15 (2018) 191–193, https://doi.org/10.1038/nmeth.4581.
[37] M. Rodahl, B. Kasemo, On the measurement of thin liquid overlayers with the quartz-crystal microbalance, in: International Conference on Solid-State Sensors and Actuators, and Eurosensors IX, Proceedings 2, 1995, pp. 743–746, https://doi.org/10.1109/sensor.1995.721939.
[38] K. Zeth, E. Hoiczyk, M. Okuda, Ferroxidase-mediated Iron oxide biomineralization: novel pathways to multifunctional nanoparticles, Trends Biochem. Sci. 41 (2016) 190–203, https://doi.org/10.1016/j.tibs.2015.11.011.
[39] B. Singh, M. Gräfe, N. Kaur, A. Liese, Applications of synchrotron-based X-ray diffraction and X-ray absorption spectroscopy to the understanding of poorly crystalline and metal-substituted Iron oxides, Dev. Soil Sci. 34 (2010) 199–254, https://doi.org/10.1016/s0166-2481(10)34008-6.
[40] F.M. Michel, L. Ehm, S.M. Antao, P.L. Lee, P.J. Chupas, G. Liu, D.R. Strongin, M.A. A. Schoonen, B.L. Phillips, J.B. Parise, The structure of ferrihydrite, a nanocrystalline material, Science 316 (2007) (1979) 1726–1729, https://doi.org/10.1126/science.1142525.
[41] D.G. Rancourt, J.F. Meunier, Constraints on structural models of ferrihydrite as a nanocrystalline material, Am. Mineral. 93 (2008) 1412–1417, https://doi.org/10.2138/am.2008.2782.
[42] A. Manceau, S. Skanthakumar, L. Soderholm, PDF analysis of ferrihydrite: critical assessment of the under-constrained akdalaite model, Am. Mineral. 99 (2014) 102–108, https://doi.org/10.2138/am.2014.4576.
[43] O. Strbak, L. Balejcikova, M. Kmetova, J. Gombos, A. Trancikova, M. Pokusa, P. Kopcansky, Quantification of iron release from native ferritin and magnetoferritin induced by vitamins b2 and c, Int. J. Mol. Sci. 21 (2020) 1–15, https://doi.org/10.3390/ijms21176332.
[44] M.G. Christiansen, N. Mirkhani, W. Hornslien, S. Schuerle, A theoretical examination of localized nanoscale induction by single domain magnetic particles, J. Appl. Phys. 132 (2022) 174304, https://doi.org/10.1063/5.0102153.
[45] J.W. Mundell, M.I. Brier, E. Orloff, S.A. Stanley, J.S. Dordick, Alternating magnetic fields drive stimulation of gene expression via generation of reactive oxygen species, IScience 27 (2024) 109186, https://doi.org/10.1016/j.isci.2024.109186.
[46] M.I. Brier, J.W. Mundell, X. Yu, L. Su, A. Holmann, J. Squeri, B. Zhang, S. A. Stanley, J.M. Friedman, J.S. Dordick, Uncovering a possible role of reactive oxygen species in magnetogenetics, Sci. Rep. 10 (2020) 1–13, https://doi.org/10.1038/s41598-020-70067-1.
[47] L. Melnikova, V.I. Petrenko, M.V. Avdeev, O.I. Ivankov, L.A. Bulavin, V. M. Garamus, L. Almásy, Z. Mitroova, P. Kopcansky, SANS contrast variation study of magnetoferritin structure at various iron loading, J. Magn. Magn. Mater. 377 (2015) 77–80, https://doi.org/10.1016/j.jmmm.2014.10.085.